AIAA AVIATION Forum
June 27-July 1, 2022, Chicago, IL & Virtual
AIAA AVIATION 2022 Forum

10.2514/6.2022-3954

Integrated Computational Aeroacoustics for UAM Design. Part 1. Farassat F1A Formulation

Vivek Ahuja*
Research in Flight, Austin, TX 78641
and
Daniel S. Little,† Joseph Majdalani,‡ and Roy J. Hartfield Jr.§
Auburn University, Auburn, AL 36849

This study focuses on the integration of established acoustic prediction techniques directly into a surface-vorticity solver. The main objective is to enhance an aircraft designer's ability to characterize the acoustic signatures generated by urban air mobility (UAM) vehicles in general, and Distributed Electric Propulsion (DEP) concepts in particular. The solver that we employ, FlightStream®, consists of a reliable, surface-vorticity panel code that incorporates viscous boundary-layer corrections. It thus constitutes a computationally efficient commercial tool developed specifically for conceptual design and preliminary aerodynamic analysis. By implementing the Farassat F1A acoustics formulation directly into the solver, a new intuitive capability is achieved, which is both conversive with modern engineering tools and efficient in terms of setup and speed of execution. In this work, this capability is demonstrated using three particular case studies consisting of both single- and six-propeller Joby S4 UAM electric vertical take-off and landing (eVTOL) as well as a Kittyhawk KH-H1 DEP vehicle. The details of this tool along with its physical characteristics and underlying equations are showcased herein whereas its acoustic metrics, which can be effectively used to characterize the noisiness of the sound generated by a UAM in flight, are described in a companion article. By embedding this assortment of insightful metrics into a simple and user-friendly flow solver, a much improved flow-acoustic analysis capability is thereby provided to support the design of future aircraft.

Nomenclature

C_f	skin friction coefficient
C_L	lift coefficient
C_p	pressure coefficient
c	speed of sound in a quiescent medium
c_0	speed of sound at temperature T_0
c_e	speed of sound at temperature T_e
DEP	Distributed Electric Propulsion
dt	time step
EPNL	Effective Perceived Noise Level
eVTOL	Electric Vertical Take-Off and Landing
FFT	Fast Fourier Transform
FAA	Federal Aviation Association
f	frequency
g_0	gravitational constant
H	shape factor, δ^*/θ
ICAO	International Civil Aviation Organization
$\boldsymbol{\ell}_i$	local force intensity component acting on fluid, $P_{ij}\hat{n}_j$
ℓ_r, $\dot{\ell}_r$	$\ell_i\hat{r}_i$, $\dot{\ell}_i\hat{r}_i$
$\boldsymbol{Ma}$	local source Mach number (vector) relative to fixed inertial frame
Ma	Mach number, $\lvert\boldsymbol{Ma}\rvert$
$\dot{M}a$	source Mach number derivative relative to source time, $\partial Ma/\partial\tau$

*CEO, Research in Flight. Senior Member AIAA.
†Graduate Research Assistant, Department of Aerospace Engineering. Member AIAA.
‡Professor and Francis Chair, Department of Aerospace Engineering. Assoc. Fellow AIAA.
§Walter and Virginia Woltosz Professor, Department of Aerospace Engineering; co-founder, Research in Flight. Assoc. Fellow AIAA.

Ma_e	boundary-layer edge Mach number
Ma_r	source Mach number in radiation direction, $Ma_i\hat{r}_i$
$\dot{M}a_r$	source Mach number derivative in radiation direction, $\dot{M}a_i\hat{r}_i$
$\hat{\boldsymbol{n}}$	outward pointing surface-normal unit vector with $\hat{n}_i$ components
OASPL	Overall Sound Pressure Level
P_{ij}	compressive stress tensor
PBS	Proportional frequency-Band Spectrum
PNL	Perceived Noise Level
PSD	Power Spectral Density spectrum
$p'(\boldsymbol{x}, t)$	static pressure
R_0	individual gas constant
r_i	radial distance from source to observer, $\lvert\boldsymbol{x} - \boldsymbol{y}\rvert_i$
SEL	Sound Exposure Level
SPL	Sound Pressure Level
T	signal period or temperature
T_0	total or stagnation temperature
T_e	boundary-layer edge temperature
t	observer time
U	freestream velocity
U_e	boundary-layer edge velocity
UAM	Urban Air Mobility
V_N	transpiration velocity normal to the surface
$\boldsymbol{v}$	velocity vector
$\boldsymbol{x}$	observer position vector with x_i components
$\boldsymbol{y}$	source position vector with y_i components

Greek Symbols

α	propeller's vertical pitch angle
δ	boundary-layer disturbance thickness
δ^*	displacement thickness
ϕ	polar angle
Φ	far-field velocity potential function
γ	ratio of specific heats
θ	azimuthal angle or momentum thickness
μ	strength of a three-dimensional point doublet
μ_0	dynamic viscosity at the stagnation temperature, T_0
μ_R	dynamic viscosity at the reference temperature, T_R
ν	kinematic viscosity
ρ	density
ρ_0	density in quiescent medium or at stagnation temperature T_0
σ	strength of a point source
τ	source time

Subscripts

0	total or stagnation term
c	compressible term
e	boundary-layer edge term
L	loading term
N	normal term
R	reference term
ret	time retarded term
T	thickness term

I. Introduction

FOR more than a decade, the emergence of Urban Air Mobility (UAM) and Distributed Electric Propulsion (DEP) vehicles [1–3] has given rise to a new platform to consider in the aerospace industry worldwide. New designs have surfaced that augment lifting capabilities using a large number of electric-motor driven propellers. Naturally, modern DEP vehicle concepts aim to realize favorable interactions between the airframe aerodynamics and the multiple electric propulsors that are strategically integrated into the airframe to achieve hitherto unrealizable gains in performance and energy consumption. Due to its novelty, the underlying paradigm shift in vehicle characteristics warrants new demands for an array of predictive capabilities. More specific to the present work, the intended urban environment for this class of vehicles places strict limitations on acoustic radiation. The corresponding limitations must be addressed at least preliminarily in the conceptual phases of design to ensure the viability of the final product. While Part 1 of this series describes the physics of incorporating aeroacoustic predictive tools into a robust flow solver, Part 2 will address the physical definitions and interpretations of the acoustic metrics that can be evaluated to support the UAM design cycle.

Due to the appreciable growth in civilian population and the number of airports and aircraft globally, the ability to predict and mitigate aircraft noise stands as a problem of tremendous significance. It continues to occupy central stage in the aircraft mobility industry in general, and the UAM research community in particular. Studies focused on the latter include, for example, those by Jia and Lee [4], Lee and Lee [5], Gwak et al. [6], Smith et al. [7], Krishnamurthy et al. [8], Jeong et al. [9], Dbouk and Drikakis [10], Ko et al. [11], and Wang et al. [12]. Evidently, to engage in the prediction of noise from a given UAM vehicle, one must begin by seeking to understand the relative contributions of the noise sources. To this end, and in the spirit of illustrating the wide range of sources that must be accounted for, particularly in what concerns the UAM vehicle category, it may be helpful to refer to the classification of noise sources according to Li and Lee [13], which is outlined concisely in Fig. 1.

It is well accepted that the most significant sources of noise for propellers with subsonic tip speeds consist of the tonal noise components of loading and thickness types [15–17]. These two primary sources of noise will therefore constitute the main focus of the present investigation and integration effort. In this process, we will also pursue a methodology that can be readily extended to perform multi-rotor DEP concept simulations to the extent of producing a conceptual-phase aeroacoustics toolbox within the solver. From a practical perspective, this choice of formulation will be quite well suited to handle the conceptual design problem as it strikes the proper balance between modeling fidelity and computational tractability, especially that it can be embodied into a dependable and fast unsteady solver [18, 19]. This unsteady solver will be relied upon to generate the unsteady aero-propulsive loads on the UAM or DEP vehicle in flight mode with spatially and temporally varying velocity fields and propeller operating conditions.

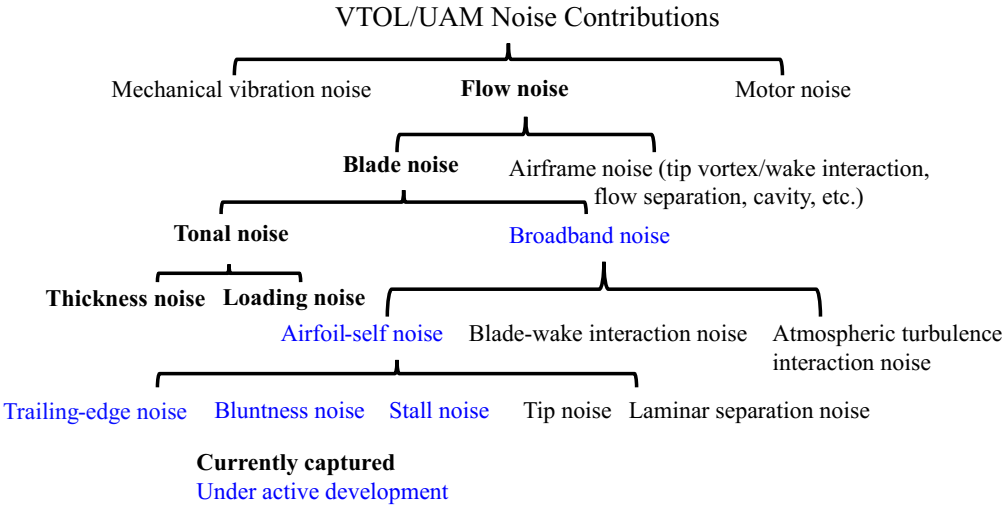

Fig. 1. Sources of noise in UAM class vehicles [14].

To address the requirement for efficient prediction of UAM noise, a novel surface-vorticity unstructured panel-method called FlightStream® will be coupled with a simplified acoustic formulation based on the Farassat 1A solution of the Ffowcs Williams–Hawkings (FW-H) equation [20]. The F1A formulation represents a viable alternative solution to the FW-H equation for thickness and loading noise computations by surface integration through the vorticity-flow solver [21]. The utilization of surface-vorticity and vortex methods in this context offers unique advantages; this has been demonstrated on several occasions by Maskew [22], Dvorak et al. [23], Maskew [24], Katz and Plotkin [25], Wu et al. [26], Ahuja et al. [14, 27], Ahuja and Hartfield [18], Faure and Leogrande [28], Faure et al. [29], and Fenyvesi et al. [30]. As for FlightStream®, several validation studies have been undertaken at the NASA Langley Research Center [31] as well as the UAM industry [18, 19, 32].

As part of prior NASA SBIR funded activities, the Research in Flight company has developed the FlightStream® flow solver to make use of surface vorticity on an unstructured surface mesh and predict loads with attached flow [18, 19]. Within its framework, aerodynamic loads are computed by shedding vorticity from the object to be analyzed and then tracked using the Fast Multipole Method (FMM). The general implementation of FMM in any fluid-flow problem revolves around coalescing far-field or potential inviscid sources and doublets into a single body for evaluation of the net effect on a near-field surface [18]. The algorithm evaluates the inductive effect of near-field bodies identically to the $O(n^2)$ implementation although it converts the large number of far-field bodies into a handful of clustered objects by taking into effect the sum total of their field strengths. Within the solver, FMM implementation condenses far-field vorticity into localized three-dimensional point doublets encompassing the net vorticity strengths of all of the coalesced far-field vorticity panels. Once the FMM near-field and far-field thresholds have been established, a spatial tree is constructed around the three-dimensional geometry to allow for the demarcation of these thresholds and to identify the near-field neighbors.

At the root of the present solver, a doublet-based vorticity scheme has been developed and implemented into FlightStream®. In this context, the spherical harmonics of degree n and order m of the overarching formulation can be expressed as

$$Y_n^m(\theta,\phi) = \sqrt{\frac{(n-|m|)!}{(n+|m|)!}}[P_n^{|m|}(\cos\theta)]e^{im\phi}, \tag{1}$$

where θ and ϕ denote the azimuthal and polar coordinates of a spherical reference frame. In the above, $P_n^m(x)$ represents the Legendre functions given by

$$P_n^m(x) = (-1)^m\left(1-x^2\right)^{\frac{1}{2}m}\frac{\mathrm{d}^m}{\mathrm{d}x^m}[P_n(x)], \tag{2}$$

and

$$P_n(x) = \frac{1}{2^n n!}\frac{\mathrm{d}^n}{\mathrm{d}x^n}\left(x^2-1\right)^n. \tag{3}$$

Let us now consider a three-dimensional point doublet with strength μ. As described by Katz and Plotkin [25], it is well known that the potential induced by a point doublet in a generalized coordinate system and its relation to a point source of strength σ can be expressed using:

$$\Phi_{\text{doublet}} = \frac{\mu}{4\pi}\hat{\boldsymbol{n}}\cdot\nabla\left(\frac{1}{\boldsymbol{r}}\right) = -\frac{\mu}{\sigma}\hat{\boldsymbol{n}}\cdot\nabla\left(-\frac{\sigma}{4\pi\boldsymbol{r}}\right) = -\frac{\mu}{\sigma}\hat{\boldsymbol{n}}\cdot\nabla\Phi_{\text{source}}. \tag{4}$$

To make further headway, the numerical solver follows the same mathematical strategy developed by Cheng et al. [33], which is outlined here for clarity. Suppose that N charges of strengths $\{q_1, q_2, \ldots, q_N\}$ are located at points $\{X_1, X_2, \ldots, X_N\}$, with spherical coordinates $(\rho_1, \alpha_1, \beta_1)$, respectively. Suppose further that the points $\{X_1, X_2, \ldots, X_N\}$ are located inside a sphere of radius a that is centered at the origin. Then, for any point $X = (r, \theta, \phi)$ with $r > a$, the potential $\Phi(X)$ generated by the doublet strengths $\{q_1, q_2, \ldots, q_N\}$ may be written as:

$$\Phi(X) = \sum_{n=0}^{\infty}\sum_{m=-n}^{n}\frac{M_n^m}{r^{n+1}}Y_n^m(\theta,\phi) \quad \text{where} \quad M_n^m = \sum_{i=1}^{N} q_i\rho_i^n Y_n^{-m}(\alpha_i,\beta_i). \tag{5}$$

Here M_n^m stands for the multipole term that combines the far-field potential functions of the individual doublet singularities whose spherical harmonics of degree n and order $-m$ is given by Y_n^{-m}. As for the radial distance, r, it extends from the center of the multipole sphere enclosing the doublet singularities to the far-field point X where the potential Φ is being evaluated.

In the context of this study, both laminar and turbulent boundary-layer models are judiciously implemented. A boundary-layer transition model is also incorporated. All of these models translate two-dimensional formulations along the on-body surface streamlines. Furthermore, due to their computational efficiency, these integral methods can be applied to any general three-dimensional wall boundary except in regions involving crossflows. The laminar boundary-layer technique used in the solver corresponds to the standard two-parameter model of the Thwaites integral method paired with the momentum integral equation [34, 35]. It is given by

$$U\frac{\mathrm{d}}{\mathrm{d}x}\left(\frac{\theta^2}{\nu}\right) = 0.45 - 6\frac{\theta^2}{\nu}\frac{\mathrm{d}U}{\mathrm{d}x}, \tag{6}$$

where U, θ, x, and ν denote the freestream velocity, momentum thickness, longitudinal streamline coordinate parallel to the surface, and kinematic viscosity. An integral boundary-layer model for compressible turbulent motion is also embodied within the inviscid-flow solver [14]. The final turbulent boundary-layer model incorporates improvements and optimizations over that of the original model developed by Standen [36]; nonetheless, it conceptually follows the formulation by Standen quite closely, thus leading to effective applications to subsonic, turbulent, and compressible motions along on-body streamlines. At its heart, the method is essentially two-dimensional and similar to the laminar model described previously, albeit extendable in a quasi-three-dimensional manner inside the solver. Moreover, in evaluating fluid properties outside the boundary-layer region, the flow is assumed to be isentropic and compressible within the subsonic regime. As such, the primary differential equations that we develop are those associated with the turbulent compressible momentum thickness, θ_c, as well as the compressible shape factor, H_c. These follow from the coupled equations:

$$\frac{\mathrm{d}\theta_i}{\mathrm{d}x} = -\frac{\theta_i}{Ma_e}\frac{\mathrm{d}Ma_e}{\mathrm{d}x}\left(2 + H_{TR}\right) + \frac{C_f}{2}\left(\frac{T_e}{T_0}\right)^3, \tag{7}$$

and

$$\frac{\mathrm{d}H_i}{\mathrm{d}x} = -\frac{\left(H_i - 0.7\right)^{3.715}}{4.17}\left[\frac{F_{\delta-\delta^*}}{\theta_i}\frac{T_e}{T_R}\left(\frac{T_e}{T_0}\right)^3\left(\frac{\mu_R}{\mu_0}\right)^{0.268} - \frac{H_{\delta-\delta^*}}{Ma_e}\frac{\mathrm{d}Ma_e}{\mathrm{d}x} - \frac{H_{\delta-\delta^*}}{\theta_i}\frac{\mathrm{d}\theta_i}{\mathrm{d}x}\right], \tag{8}$$

where

$$H_{TR} = \frac{T_w}{T_0}H_i + \frac{T_{aw}}{T_0} - 1 \quad \text{and} \quad F_{\delta-\delta^*} = 0.03268\left(H_{\delta-\delta^*}\right)^{-1.3} + 0.006. \tag{9}$$

In the above, C_f, θ_i, H_i, H_{TR}, $H_{\delta-\delta^*}$, $F_{\delta-\delta^*}$, and Ma_e represent, sequentially, the skin friction coefficient, the incompressible momentum thickness, the incompressible shape factor, the transformed shape factor, the entrained shape factor, the non-dimensional mass entrainment rate, and the Mach number at the boundary-layer edge. Moreover, T_0, T_{aw}, T_w, T_R, and T_e refer to the total stagnation temperature in the far-field, the adiabatic wall temperature, the wall temperature, the reference temperature, and the static temperature at the boundary-layer edge, consecutively. Lastly, δ and δ^* stand for the compressible boundary-layer disturbance and displacement thicknesses, whereas μ_0 and μ_R denote the dynamic viscosity at T_0 and T_R, respectively. Given the number of unknowns, three auxiliary relations are still required to achieve closure. These include the definition of the Mach number, the derivative of the Mach number along a streamline, and the definition of the shape factor. As shown by [36], these can be retrieved from:

$$Ma_e = \frac{U_e}{\sqrt{\gamma g_0 R_0 T_e}}, \tag{10}$$

$$\frac{\mathrm{d}Ma_e}{\mathrm{d}x} = \frac{1}{c_e}\left[1 + \frac{U_e\left[\left(\gamma - 1\right)T_e^2 Ma_e\right]}{2c_e T_0 T_e}\right]^{-1}\frac{\mathrm{d}U_e}{\mathrm{d}x}, \tag{11}$$

$$H_{\delta-\delta^*} = 1.5359\left(H_i - 0.7\right)^{-2.715} + 3.4, \tag{12}$$

and

$$\frac{C_f}{2} = \left[0.123\, e^{-1.56H_i}\left(U_e\theta_i\frac{\rho_0}{\mu_0}\right)^{-0.268}\right]\left[\frac{T_e}{T_R}\left(\frac{T_R}{T_0}\right)^{0.402}\left(\frac{T_0 + 198}{T_R + 198}\right)^{0.268}\right]. \tag{13}$$

The additional parameters, U_e, c_e, γ, g_0, R_0, and ρ_0 allude to the far-field velocity at the edge of the boundary layer, the sound speed at the edge of the boundary layer, the ratio of specific heats, the gravitational constant, and the individual gas constant. In practice, the resulting equations can be readily solved numerically for all relevant boundary-layer characteristics using, for instance, a conventional 4th-order Runge–Kutta scheme along the on-body streamlines.

It can thus be seen that, with the integration of modern viscous models, several computational enhancements are added to the solver. This is accomplished while still maintaining an $O(n \log n)$ scalability to the performance of the boundary-layer algorithms. To this end, spatial octree algorithms that mimic the existing FMM implementation within the inviscid solver are extended to the viscous near-wall regions. This extension leads to rapid near-field sorting of points that are closest to or inside a viscous-flow region. The corresponding octree-based volume grid, termed the viscous spatial tree (VST), is refined to capture the three-dimensional volume of the boundary-layer region extending above the surface of the geometry. Following this corrective implementation, the VST increases the memory footprint of the otherwise inviscid solver by less than 5% for all cases considered. However, the performance benefits are substantial: in lieu of an anticipated $O(n \times m)$ algorithm, where m denotes a very large integer corresponding to the total number of surface mesh faces, we essentially arrive at an appreciable reduction to $O(n \log n)$ [14].

Apart from these boundary-layer refinements, a robust model for computing attachment lines and critical points on the inviscid surface velocity fields is integrated into the solver. This particular step enables us to systematically retain the flow coupling with the viscous boundary-layer models described previously. In practice, the laminar and turbulent boundary-layer formulations are embedded within the inviscid solver via displacement of the inviscid boundary by an equal amount to the displacement thickness of the local boundary layer. The latter indicates the extent to which the surface has to be displaced in order to permit the same flow rate as the viscous motion while using an inviscid velocity profile. The conventional displacement thickness concept can therefore be used to predict the required displacement of the inviscid boundary. Presently, the inviscid boundary displacement is simulated by a transpiration flow boundary condition that is added to the inviscid Neumann-type constraint normal to the mesh face. The magnitude of the transpiration velocity, V_N, can be computed rather straightforwardly using the momentum flux equation [14]. It is given by

$$V_N = -\frac{\partial \left(U_e \delta^*\right)}{\partial s}, \tag{14}$$

where δ^* denotes, as usual, the displacement thickness based on the integral boundary-layer computations; on the other hand, U_e stands for the local streamline velocity outside the boundary layer, and s represents the direction along the local surface. Equation (14) can be computed for the transpiration velocity V_N along the on-body streamlines for each mesh face using standard finite-difference numerical marching schemes.

II. Acoustics Modeling

A. Theory

Over the years, NASA has created, or has had access to, a variety of high-order acoustics formulations both for use with potential-theory solvers, as well as conventional Navier–Stokes CFD solvers. Tools such as WOPWOP, WOPWOP+ [37, 38], ANOPP2 [39], ASSPIN [40], and others [41, 42] have provided very powerful acoustic analysis capabilities. In most cases, however, they have lacked a user-friendly interface or a convenient post-processing toolbox to encourage their adoption by the non-specialists. Gradually, these tools have been refined to incorporate the high-order nonlinear terms into the acoustics framework. To clarify, it may be helpful to illustrate through superposition the various acoustic components that make up the total acoustic signal at an observer location at a given time. One can put:

$$p'(\boldsymbol{x}, t) = \left[p'_T(\boldsymbol{x}, t) + p'_L(\boldsymbol{x}, t)\right] + p'_Q(\boldsymbol{x}, t) + p'_{NL}(\boldsymbol{x}, t), \tag{15}$$

where p' represents the acoustic pressure, $\boldsymbol{x}$ denotes the observer position relative to the source, and t refers to the observer's time. In the above equation, the term $p'_Q(\boldsymbol{x}, t)$ relates to the acoustic quadrupoles while the $p'_{NL}(\boldsymbol{x}, t)$ term captures the correction due to nonlinear effects. The first two terms, $p'_T(\boldsymbol{x}, t)$ and $p'_L(\boldsymbol{x}, t)$, correspond to the thickness and loading components of the acoustic signature at the observer's location.

It should be noted that the noise due to compressibility effects is typically accounted for in a third term, namely, the *quadrupole* noise source. In the present implementation, the *quadrupole* noise source is not considered because it reflects a volume source that requires a grid-based Navier–Stokes flow solver; as such, it will be quite expensive to evaluate in early design workflows. In fact, the volume integral of quadrupole sources that arises in the nonlinear region outside of an acoustic control surface presents a major challenge and adds significant complexity to the acoustics models. However, if we were to ignore the quadrupole and nonlinear terms, the resulting framework reduces the necessary calculations by one order of magnitude, specifically, by lowering the order of the acoustic solution. Similarly, if the nonlinearities on the control surface are ignored, the acoustics computations assume a solution to the linear wave

equation on the surface. From a practical perspective, and for both DEP and UAM flight vehicles, especially in early design stages, the nonlinearities can be reasonably ignored. At the outset, the total signature equation turns into the sum of the thickness and loading terms,

$$p'(\boldsymbol{x},t) = p'_T(\boldsymbol{x},t) + p'_L(\boldsymbol{x},t)\,. \tag{16}$$

On the one hand, the thickness noise source p'_T accounts for noise due to the displacement of the fluid by the finite thickness of the body. On the other hand, the loading noise source p'_L accounts for noise due to loading and change of loading on the body. The typical starting point for any numerical noise prediction algorithm attempting to solve for the thickness and loading terms follows from one of the various forms of the solution to the Ffowcs Williams–Hawkings (FW-H) equation [20]. In the present work, the FW-H equation for a *permeable surface* is employed. This is known as *Formulation 1A* and yields the following equations for the thickness and loading terms [21]:

$$4\pi p'_L(x,t) = \frac{1}{c}\int_{f=0}\left[\frac{\dot{\ell}_i\hat{r}_i}{r(1-Ma_r)^2}\right]_{\text{ret}}\mathrm{d}S + \int_{f=0}\left[\frac{\ell_r-\ell_i Ma_i}{r^2(1-Ma_r)^2}\right]_{\text{ret}}\mathrm{d}S + \frac{1}{c}\int_{f=0}\left[\frac{\ell_r\left(r\dot{M}a_i\hat{r}_i + cMa_r - cMa^2\right)}{r^2(1-Ma_r)^3}\right]_{\text{ret}}\mathrm{d}S, \tag{17}$$

and

$$4\pi p'_T(x,t) = \frac{1}{c}\int_{f=0}\left[\frac{\rho_0 v_n\left(r\dot{M}a_i\hat{r}_i + cMa_r - cMa^2\right)}{r^2(1-Ma_r)^3}\right]_{\text{ret}}\mathrm{d}S, \tag{18}$$

where

$$\boldsymbol{r} = \boldsymbol{x}-\boldsymbol{y}, \quad \hat{\boldsymbol{r}} = \frac{\boldsymbol{r}}{|\boldsymbol{r}|}, \quad Ma_i = \frac{v_i}{c}, \quad Ma_r = \frac{Ma_i r_i}{r} = Ma_i\hat{r}_i, \quad \dot{M}a = \frac{\partial Ma}{\partial\tau}, \quad \text{and} \quad \ell_r = \frac{\ell_i r_i}{r} = \ell_i\hat{r}_i. \tag{19}$$

In this formulation, $\hat{\boldsymbol{r}}$ corresponds to the unit vector in the direction of acoustic wave radiation, whereas $v_n = v_i\hat{n}_i$ consists of the local normal velocity on the actual surface. As for the remaining terms, they are specified one-by-one in the Nomenclature.

In the present solver, these equations are integrated using the time-dependent aerodynamic data and the corresponding derivatives are generated by the unsteady solver. The rotor blades are discretized into panel elements within the solver, each of which being an acoustic source. In this process, the loading noise is calculated based on the loading and velocity of each element. The thickness noise term is dependent on v_n, the blade's local normal velocity. The loading and thickness noise contributions of all elements are then collected to deduce the total acoustic noise signal at user-defined measurement points [16, 17].

It may be instructive to note that, in the loading and thickness expressions, integrands with r^{-1} dependence denote far-field terms that decay rather slowly, whereas those with r^{-2} dependence constitute near-field terms that dissipate quite precipitously. Although the integrands in Formulation 1A are somewhat more complicated than in Formulation 1, a numerical differentiation of an integral is no longer required. This is especially beneficial for cases where the observer is moving.

To facilitate the implementation of Formulation 1A, the retarded time computation scheme chosen for this work will be based on the source-time-dominant model described, for example, by Brentner and Farassat [17]. This model considers the source time as the primary or dominant time. Rather than select the observer time in advance, one can choose the source time for a panel "i" by again using each panel's center, and determine when the signal will reach the observer. If the observer $\boldsymbol{x}$ happens to be stationary, then one must have,

$$t\ (\text{observer time}) = \tau\ (\text{source time}) + r_i/c. \tag{20}$$

In the above, r_i denotes the radial distance from the acoustic source (located at $\boldsymbol{y}_i$) to the observer (at $\boldsymbol{x}$), whereas t and τ refer to times measured at the observer and source locations, respectively. In most cases, this time projection can be computed immediately. Otherwise, one can extract the root of

$$t - \tau - \frac{\left|\boldsymbol{x}(t) - \boldsymbol{y}_i(\tau)\right|}{c} = 0. \tag{21}$$

The determination of t even for the latter case is easier than finding the retarded time because the observer motion is usually simple to track; in this event, the solution for t may be found analytically rather than by iteration. A sequence

of source times (i.e., the times at which the source strength is available) will ultimately lead to a sequence of unequally spaced observer times. This panel time history can then be interpolated to provide the proper contribution of each panel to the net acoustic signal as seen at the observer location. Interpolation in time is subsequently undertaken in order to consolidate the signal contributions originating from all source panels at the same observer times.

This foregoing algorithm has the unique advantage that a retarded-time calculation is not necessary *per-se* and that the discrete time-dependent input data sets do not need to be interpolated. This characteristic can be very beneficial, especially when the FlightStream® solver itself is being relied upon to generate the input data internally and seamlessly. Another computational advantage of the source-time-dominant algorithm can be ascribed to the solution process being inherently parallel; in fact, the algorithm proves to be an excellent candidate for parallel computing. Performance tests performed by Metzger [37] confirm that the source-time-dominant algorithm requires significantly fewer operations for a maneuvering vehicle prediction. Lastly, although an effort has been made to investigate quadrupole term implementation, it has not been further pursued based on the knowledge that most UAM vehicles are not expected to fly in regimes where quadrupole terms become appreciable or even measurable.

B. Acoustic Fields

1. Volume Sections

Acoustic volume sections are planar grids of stationary microphones placed in any arbitrary orientation, size, and resolution around a vehicle being simulated using the FlightStream® unsteady flow solver. The volume section can be used to generate a contour of sound pressure-time history that can then be exported and analyzed for acoustic volume field effects rather than point effects for a single stationary observer. Examples of acoustic volume sections are shown in Fig. 2 for a representative vehicle. This is based on the Open Vehicle Sketch Pad (OpenVSP) geometric file of a NASA Revolutionary Vertical Lift Technology (RVLT) Tiltwing UAM electric Vertical Take-Off and Landing (eVTOL) concept. This particular RVLT vehicle is powered by eight 5-bladed propellers operating at 1420 RPM and a tip Mach number of 0.5. The vehicle is simulated in forward-flight mode at a zero angle of attack and a cruise speed of 20 m/s. In Fig. 2, the outer radius of the acoustic volume section is set at 50 m and the grid resolution is taken to be 40×40 in the radial and azimuthal directions, respectively.

Figure 2 clearly illustrates the nature of the acoustic field around the vehicle using an orthogonal XYZ coordinate system; therein, the horizontal X and Y axes run parallel to the fuselage and wings, respectively, and Z stands vertically, i.e., normally to the planform area. In the XY plane (top view in Fig. 2a), the strong signal characteristics are visible in the section located 3 m below the vehicle's centroid. By the time that the signal reaches 20 m below the vehicle, the signal becomes quite faint (Fig. 2b). Also visible are the strong signals engendered near the tips of the propeller rotor discs, as seen in the YZ and XZ section fields of Figs. 2c and 2d. Note the phase change of the signal strength upstream and downstream of the rotor disc. Interestingly, an acoustic noise "bubble" develops around the vehicle near-field in the YZ plane, namely, 5 m upstream of the vehicle's centroid, where it just touches the nose of the vehicle (Fig. 2c). These visual characteristics are complemented by the side view of the aircraft, which is taken 5 m to the left of the vehicle (Fig. 2d). At this juncture, one may recall from Sec. II.A that the acoustic shielding effects off the fuselage are not presently modeled. This explains, in part, the clean nature of the noise bubble around the vehicle. In fact, acoustic scattering constitutes another mechanism that is not implicitly captured by the present implementation. In the companion study, the Fast Fourier Transform (FFT) functions for the present acoustic fields are discussed along with the metrics for determining the Overall Sound Pressure Level (OASPL), Sound Exposure Level (SEL), Power Spectral Density (PSD) spectrum, Proportional frequency-Band Spectrum (PBS), Perceived Noise Level (PNL), and Effective Perceived Noise Level (EPNL), to name a few.

2. Acoustic Spheres

Acoustic spheres surrounding an object to be modeled constitute a direct extension of the acoustic volume section concept, although they seem to allow for more detailed volumetric signal field analysis. The acoustic sphere is added as yet another user-controlled step for post-processing in FlightStream®. As in the case of the acoustic volume sections, the acoustic sphere can be placed in any arbitrary orientation, size, and resolution around a vehicle being simulated using the unsteady flow solver. Moreover, as done previously with volume sections, a sphere can be used to generate vivid contours of sound pressure-time history that can be subsequently exported and analyzed for acoustic volume field effects rather than just point effects for a single stationary observer. Examples of acoustic spheres are provided in Sec. III below.

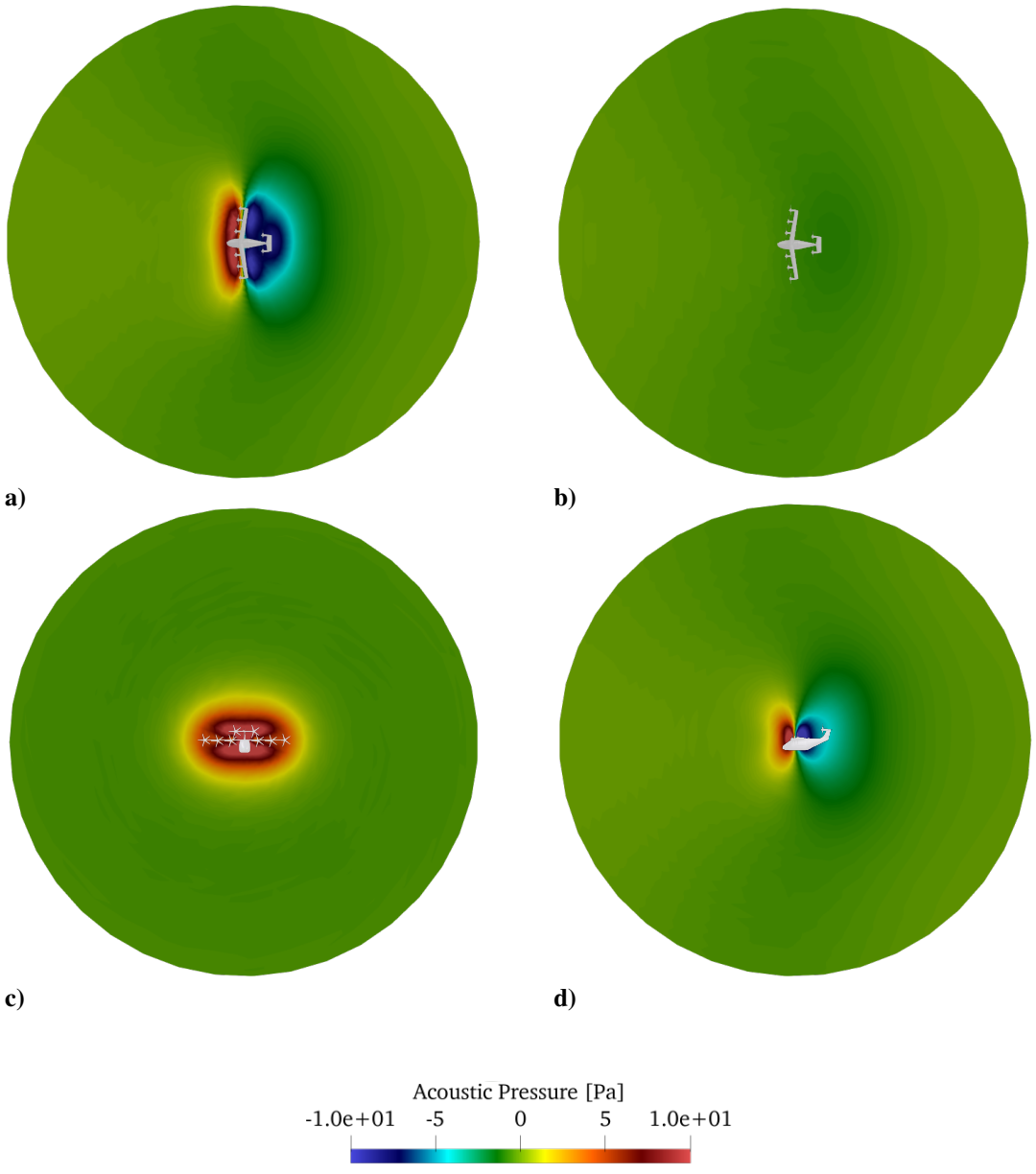

Fig. 2. Acoustic sections around a contemporary NASA RVLT Tiltwing UAM eVTOL concept in forward-flight mode using an outer radius of 50 m: a) Plane XY, 3 m below vehicle's centroid; b) Plane XY, 20 m below vehicle; c) Plane YZ, 5 m in front of the vehicle; and d) Plane XZ, 5 m left of vehicle.

III. Results

A. Validation

Since one of the key objectives of this effort is to demonstrate that the methods chosen for implementation are reasonably accurate and viable for use in early design analysis, it is useful to verify the numerical implementation through comparisons to the experimental data already at hand for the UH-1H rotor [39]. Acoustic data predictions for this rotor are available through both WOPWOP and experimental measurements obtained by Conner and Hoad [39].

Although the UH-1H rotor is described in detail by Conner and Hoad [39], it can be summarized as a twin blade teetering rotor system with a NACA 0012 airfoil; for this case study, the collected measurements correspond to hover and forward-flight conditions. More specifically, data is acquired at microphones that are positioned at various locations from the rotor hub [38]. The rotor outer radius of the 1:4 scale model is 1.829 m. The rotor blade has a pre-twist of -10.9° that is distributed linearly. The blade is then provided with a 15° pitch and a 2° coning angle. Lastly, the rotor speed is measured at 1296 RPM and the geometry is tested at standard atmospheric conditions.

In this study, hover tests are conducted in FlightStream® to verify acoustic predictions of the solid-blade UH-1H rotor against available data from the original version of WOPWOP [38]. To this end, the microphone used for measuring the signals in hover is placed at a distance of 3 m in the plane of the rotor, away from the hub. The acoustic pressure history from FlightStream® is then post-processed into a normalized timescale using the blade period as a reference. The resulting vorticity contour lines are shown in Fig. 3. Note that FlightStream® simulation runs do not exceed 1-3 minutes including the acoustic data processing time. In the hover tests, the comparison with WOPWOP results in

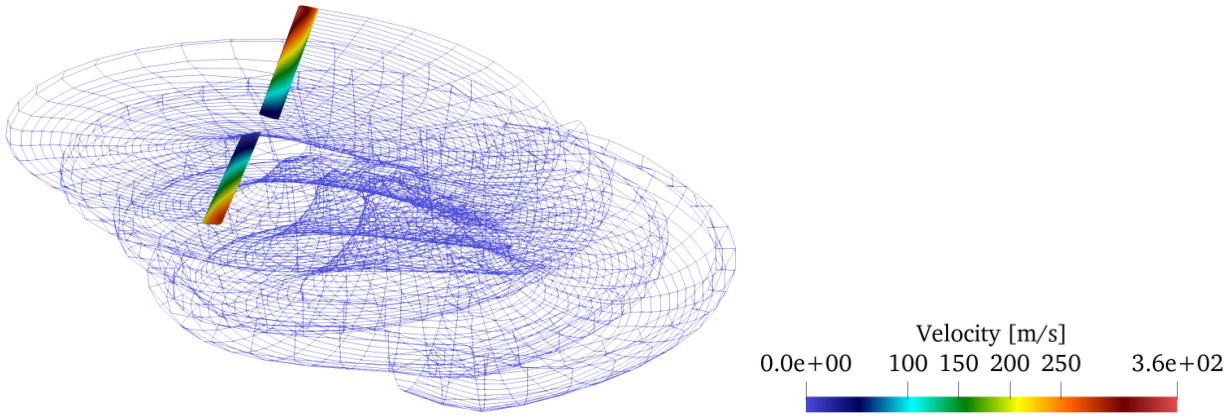

Fig. 3. UH-1 helicopter rotor in showing normalized surface-vorticity contours as computed for hover.

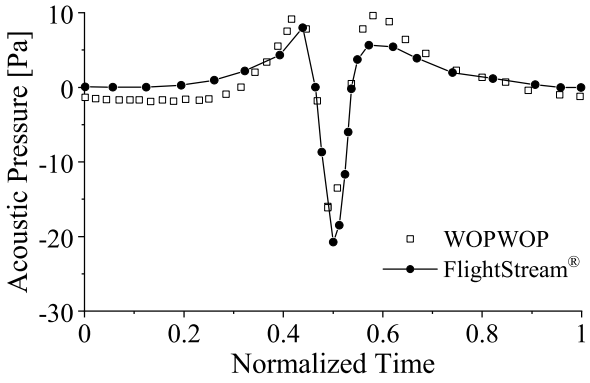

Fig. 4. UH-1H helicopter rotor in hover: overall sound pressure history vs. time normalized by the propeller blade period.

Fig. 4 is rather compelling and supportive of the validity of the acoustic analogy formulation implemented heretofore. The reason for the differences between the original WOPWOP results and the present implementation can be attributed to inevitable dissimilarities in the numerical schemes, grid refinements, and the geometry itself: the present solver uses a solid propeller blade with viscous boundary-layer coupling, as specified through Eqs. (6–14) .

Besides hover flow analysis, forward-flight tests are performed using an advance ratio of 0.208 and an 8.85° forward disc tilt, with predictions being compared against the data from Conner and Hoad [39] in Fig. 5. Here too, forward-flight microphones are placed at a distance of 4 m upstream of the hub and in the plane of the rotor itself. More specifically, one microphone is placed near each of the advancing and retreating blades. In both cases, an overall trend is captured by this simplified implementation. Nonetheless, the high-frequency components present in the experimental results are not captured by either the current methodology or by WOPWOP [38]. While some of the high frequency contributions may be due to experimental noise, it is suspected that some of the oscillations may be caused by the flexibility of the blades or else attributable to compressibility effects.

B. Case 1: Full UAM Vehicle with Isolated Propeller

To further establish the robustness and sensitivity of the present aeroacoustics formulation in FlightStream®, three different numerical case studies are undertaken. The first of these focuses on a single 5-bladed propeller that is mounted on a contemporary UAM vehicle, as shown in Fig. 6. The UAM vehicle chosen for this example corresponds to the publicly-available NASA OpenVSP model of the Joby S4 UAM eVTOL vehicle. The model is transferred from OpenVSP to FlightStream® as a Plot3D geometry with both solid and thin-surface representations of the propeller blades. The fuselage, wings, and nacelles are Boolean-united in OpenVSP before transfer. The propeller is operated at 955 RPM and $\alpha = 0°$ while the tip Mach number is set at $Ma = 0.4$.

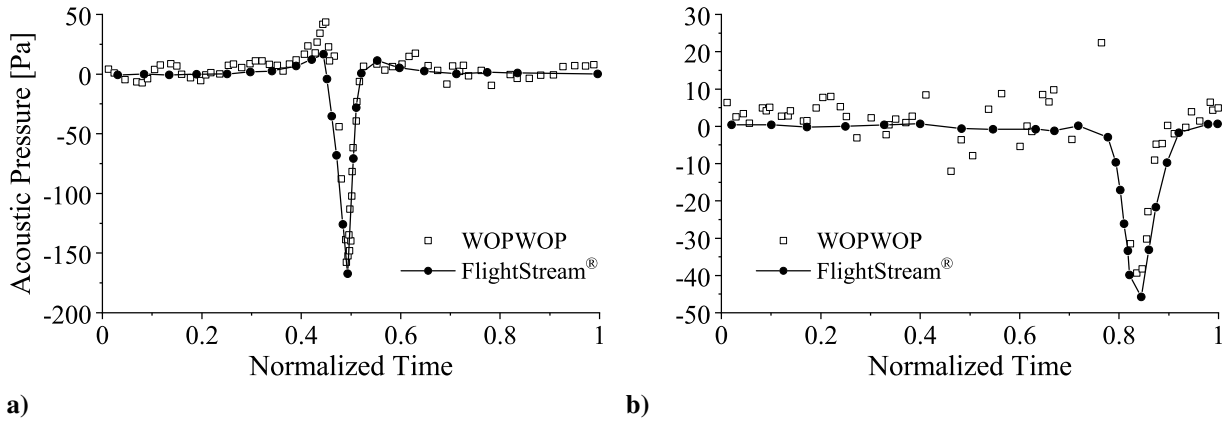

Fig. 5. UH-1H helicopter rotor in forward flight: overall sound pressure history vs. time normalized by the propeller blade period. Results correspond to a) NASA TM-84553, MIC4 and b) NASA TM-84553, MIC5.

Fig. 6. Joby S4 UAM eVTOL vehicle with a single operating 5-bladed propeller in forward-flight mode (Case 1).

Throughout these simulations, the observer time signal window is taken to be approximately 0.15 s. Moreover, in what concerns this case study as well as the ones to follow, the full two-way aerodynamic coupling is maintained between the overall vehicle and the propeller, as part of the unsteady aerodynamic flow solutions. However, the absence of an acoustic shielding model implies that the acoustic signal emanating from the propeller blades remains unaffected by the shielding effects of the vehicle relative to the observer. In practice, this leads to unrestricted pressure wave propagation through the domain. As for the acoustic shielding and scattering modeling effects, they are hoped to be explored in future work.

The acoustic signal histories are generated at 36 microphones that are placed in the form of a circular array at a range radius of 50 m within the plane of the propeller and centered about the propeller hub. Each microphone is separated from its neighbor by an azimuthal angle of 10°. For each observer, a pressure-time signal is recorded and analyzed to the extent of retrieving the Overall Sound Pressure Level (OASPL) at each observer location. Subsequently, pressure signals obtained at various angular positions are collected and displayed in Fig. 7.

According to this angular distribution, the flow is directed along the 180° → 0° line into the propeller, which is facing 180°. At first glance, several key characteristics may be inferred from these results. Firstly, the acoustic pressure signal distribution changes azimuthally around the propeller. Secondly, the minimum signal magnitude is obtained in the front and rear of the propeller, whereas the maximum values appear in the tip plane of the propeller disc. Deviations between these two extremes can be seen in Fig. 7. Note that the numerical error in the acoustic signal is dominant at both 0° and 180° azimuthal locations, with no physical signal profile visible. At 90°, strong sinusoidal signals that correlate with the operating RPM of the propeller are observed. These results are consistent with the response of a single propeller in acoustic isolation [17].

As described in Sec. II.B.1, and further illustrated in Fig. 2, one can rely on so-called acoustic volume sections, which consist of planar arrays of stationary microphones that are distributed around the vehicle, using well-delineated shapes, sizes, and resolutions within FlightStream®. The acoustic field around the vehicle can then be deduced from the resulting contours of sound pressure-time histories obtained across these sections.

For the Joby S4 UAM eVTOL vehicle with a single propeller, an outer radius of 15 m is used to delimit the acoustic field, as shown in Fig. 8. This enables us to visualize the sound pressure distribution around the vehicle while the propeller is operating in forward-flight mode. For example, the top view section given by Fig. 8a, which corresponds

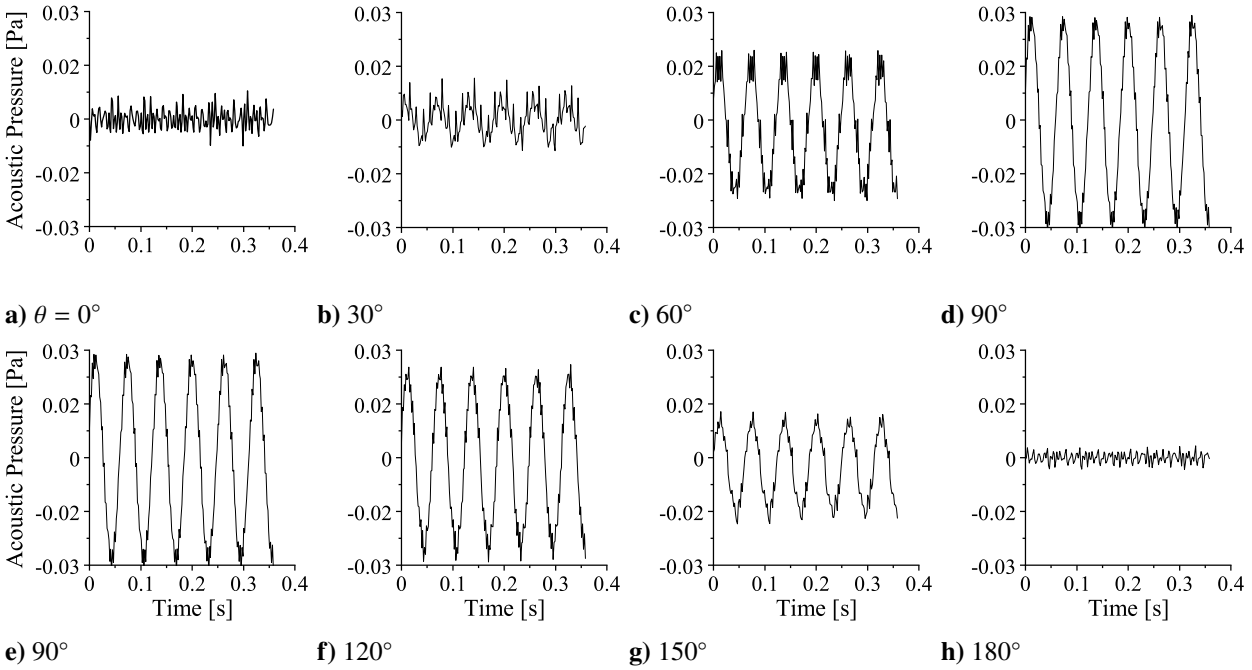

Fig. 7. Joby S4 UAM eVTOL vehicle with a single operating 5-bladed propeller in forward-flight mode (Case 1). Acoustic pressure [Pa] signals at a 50 m radius from the propeller hub are shown specifically at a) θ = 0°, b) 30°, c) 60°, d) 90°, e) 90° (second row), f) 120°, g) 150°, and h) 180°.

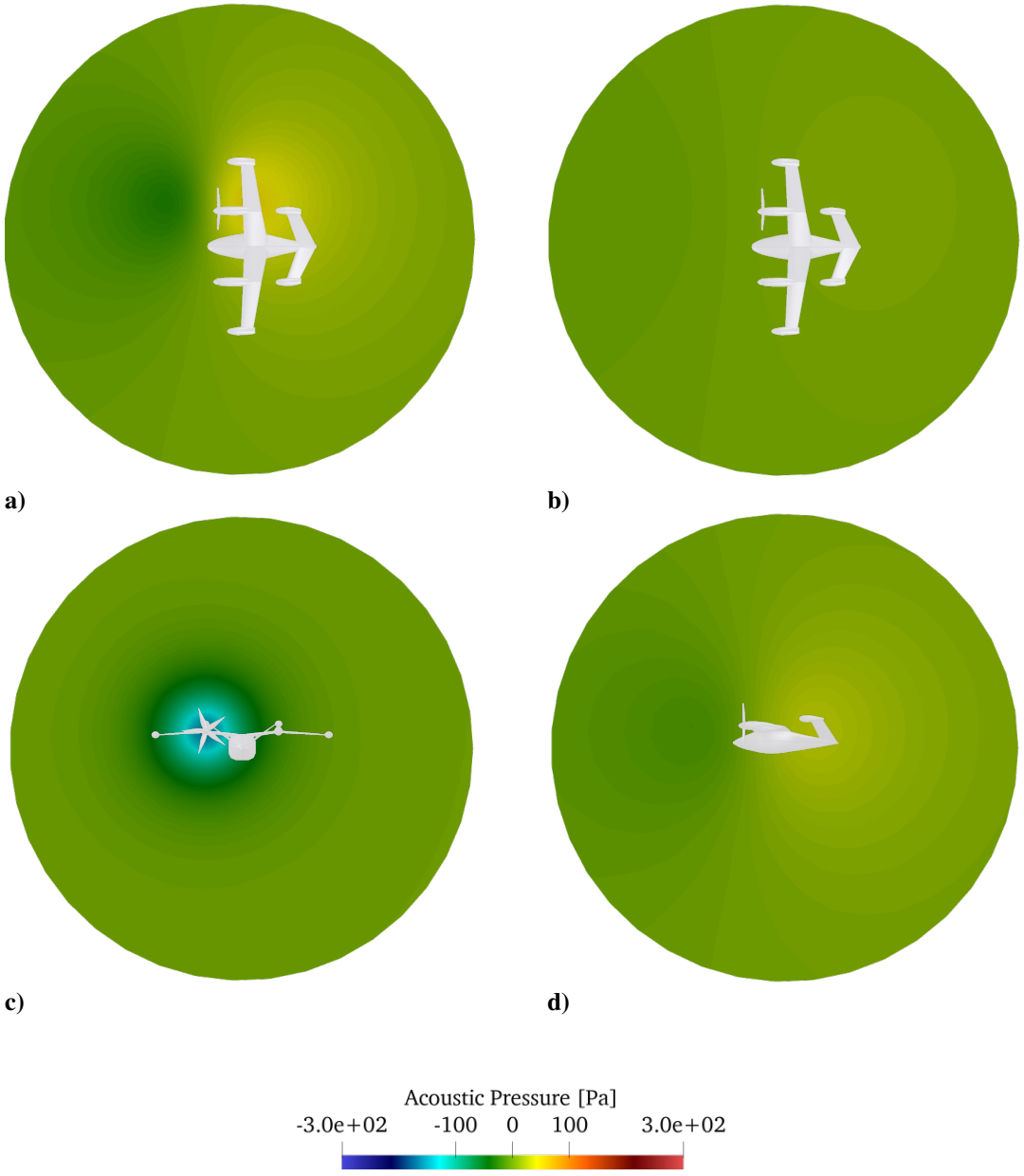

Fig. 8. Acoustic sections around a Joby S4 UAM eVTOL vehicle with a single 5-bladed propeller operating in forward-flight mode using an outer radius of 15 m: a) Plane XY, 5 m below vehicle's centroid; b) Plane XY, 10 m below vehicle; c) Plane YZ, 3 m in front of the vehicle; and d) Plane XZ, 8 m left of vehicle.

to an XY plane taken at a distance of 5 m below the vehicle's centroid, the sound concentration around the propeller in operation can be clearly seen. However, as the distance from the propeller is doubled to 10 m, the signal is weakened to the extent of becoming barely visible, being masked by the background noise (Fig. 8b). The front view of the vehicle, which is given by Fig. 8c, clearly shows the circular sound bubble generated by the propeller in the YZ plane taken 3 m upstream of the vehicle, with the strongest signals around the tips of the rotor disc and dissipating radially outwardly. These results are complemented by the XZ section field in Fig. 8d, where a side view of the aircraft taken 8 m leftward helps to identify the dissimilarities in signal strength distribution around the vehicle. Given the present cruising speed, the sound generated by the propeller may be seen to trail downstream behind the rotor disc and then dissipate spherically outwardly.

C. Case 2: Full UAM Vehicle with Multiple In-Phase Propellers

The next case study enables the remaining five propellers on the UAM vehicle to operate, thus illustrating the typical multi-rotor forward-flight DEP and eVTOL industry applications. To do so, all six propellers are operated synchronously in forward-flight mode at 955 RPM and a tip Mach number of 0.4. The corresponding UAM vehicle configuration is shown in Fig. 9. The FlightStream® flow solution, which is provided in Fig. 10, depicts very distinct vortex stream formations from the interacting propellers. Note that all of the propeller wakes and geometric details are aerodynamically coupled with the fuselage, nacelles, and wings. In this vein, the wake interference from the front rotor onto the rear rotor can be viewed in Fig. 10.

Once again, 36 stationary microphones are placed in the form of a circular array at three specific radii of 50 m, 100 m, and 150 m, respectively; these are placed in a plane 4 m below the base of the vehicle fuselage and centrally with respect to the computed centroid of the vehicle. Each microphone is separated from its neighbor by an azimuthal angle of 10°. For each observer, a pressure-time signal is recorded and analyzed to retrieve OASPL values at each observer location. These are collected and then displayed in Fig. 11, where several pressure signals measured at 30° intervals are shown. As before, the flow runs parallel to the 180° → 0° line into the propeller, which faces toward the 180° position.

As expected, the loudest signal is observed at right angles to the propeller blades while looking at the tips of the blades. However, the flow signals are now substantially different from those obtained in Case 1 for an acoustically isolated propeller. The net signal at these locations reflects the acoustic in-phase and out-of-phase coupling of the six independent propeller signals. It is noteworthy that the signal in front of the vehicle at 180° has a mean-zero signal magnitude with the exception of smaller signal spikes at 0.06 s and 0.09 s; these correspond to the in-phase periodic summation of the propeller signals. A more washed-out signal in the opposite direction can be seen at the rear of the vehicle around 0°. We also note the spikes in the peak signal time positions at the 90° location due to the signal travel time to the observer from the six spatially separated propellers. It should be recognized that most of the tonal power stems from the propeller's RPM, with secondary contributions from harmonics related to the blade passage frequency.

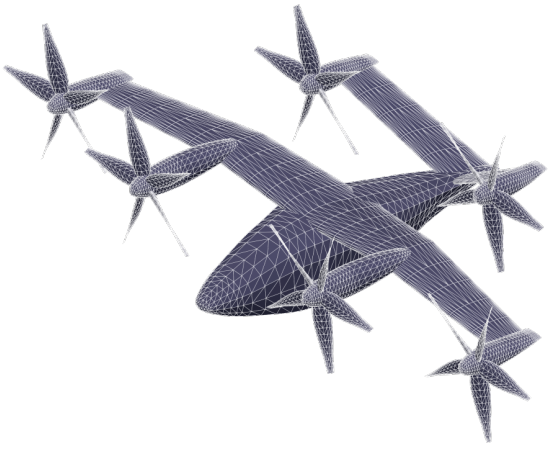

Fig. 9. Joby S4 UAM eVTOL with all six 5-bladed propellers operating synchronously in forward-flight mode (Case 2).

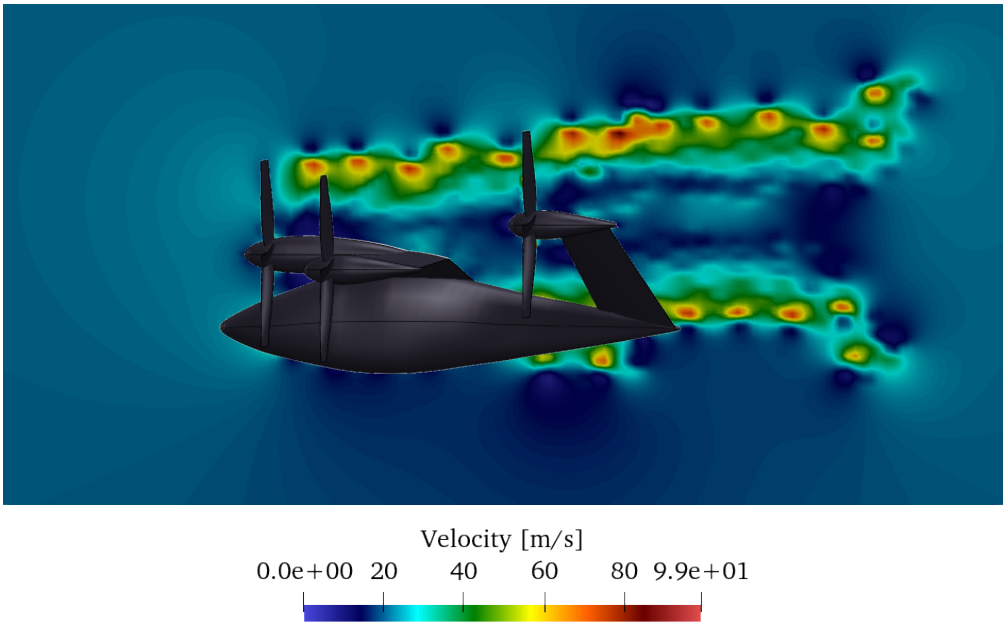

Fig. 10. FlightStream® simulations: Joby S4 UAM eVTOL vehicle with all six 5-bladed propellers operating synchronously in forward-flight mode (Case 2). Rotors are set at 955 RPM with α = 5° and a tip Mach number of Ma = 0.4.

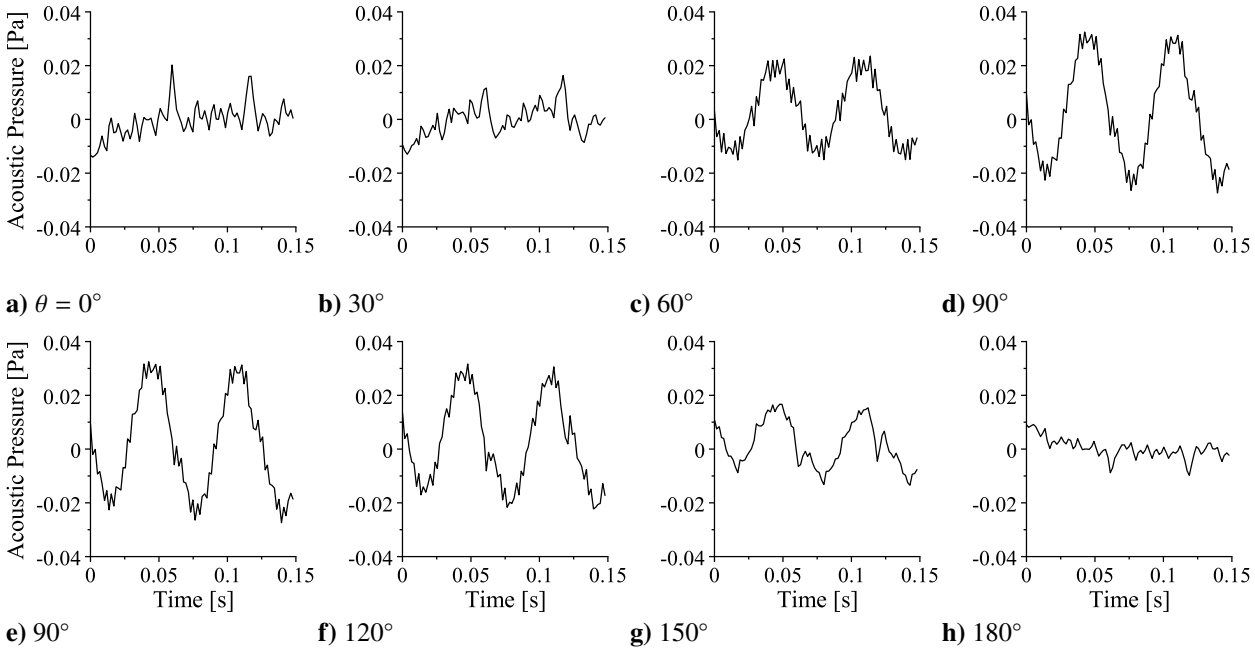

Fig. 11. Joby S4 UAM eVTOL vehicle with all six 5-bladed propellers operating in forward-flight mode (Case 2). Acoustic pressure [Pa] signals provided at various distances from the vehicle's centroidal location are shown specifically at a) θ = 0°, b) 30°, c) 60°, d) 90°, e) 90° (second row), f) 120°, g) 150°, and h) 180°.

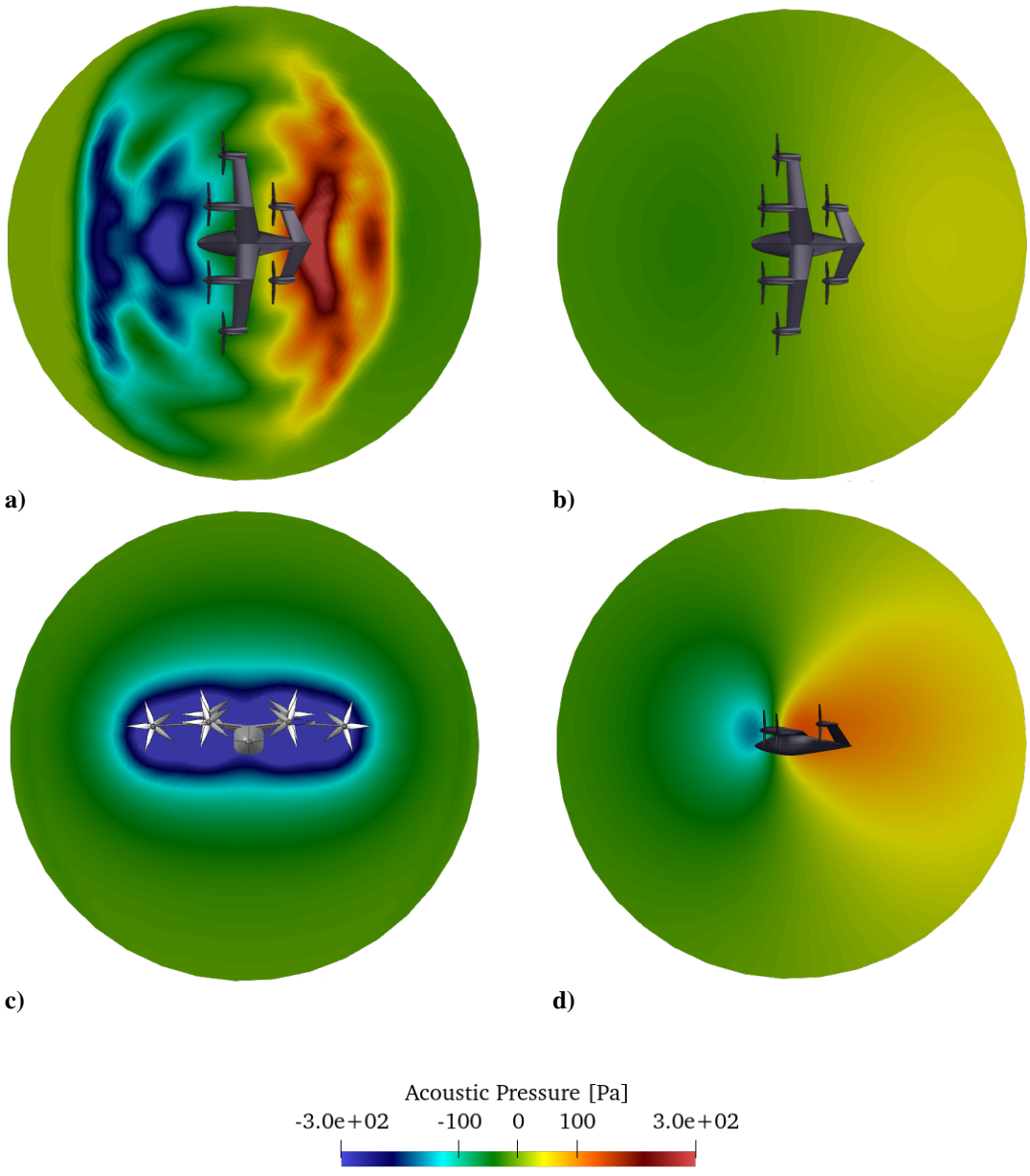

Fig. 12. Acoustic sections around a Joby S4 UAM eVTOL vehicle with all six 5-bladed propellers operating synchronously in forward-flight mode using an outer radius of 15 m: a) Plane XY, 5 m below vehicle's centroid; b) Plane XY, 10 m below vehicle; c) Plane YZ, 3 m in front of the vehicle; and d) Plane XZ, 8 m left of vehicle.

In this case, as with the first case, spikes are detected along multiples of the blade passage frequency.

Having examined the acoustic pressure signal at discrete points and the vortex stream formations around the vehicle, we now turn attention to the acoustic field distribution surrounding the vehicle. Similarly to Case 1, the actual field can be visualized using acoustic volume sections, as shown in Fig. 12. Of particular note here is that, in the XY plane (top view in Fig. 12a), the strong signal characteristics are visible in the section located 5 m below the vehicle's centroid. By the time the signal reaches 10 m below the vehicle, the signal dissipation becomes quite visible (Fig. 12b). Also visible are the strong signals engendered near the tips of the propeller rotor discs, as seen in the YZ and XZ section fields of Figs. 12c and 12d. Note the phase change of the signal strength upstream and downstream of the rotor disc. Furthermore, and as we have seen before, an acoustic noise bubble develops around the vehicle near-field in the YZ plane, 3 m upstream of the vehicle's centroid, where it just touches the nose of the vehicle (Fig. 12c). These visual characteristics are complemented by the side view of the aircraft, which is taken 8 m to the left of the vehicle (Fig. 12d).

Besides flow visualization using acoustic sections, the solver is now augmented with the ability to produce cutaways of acoustic spheres. These are showcased in Fig. 13, where two acoustic spheres are generated around the Joby vehicle in forward flight. In this example, all six 5-bladed propellers are set in synchronous operation and the images depict two instants of time, particularly, $t = 0.04$ s and 0.1 s. Moreover, acoustic pressure values (in Pascals) are shown on the surface of the spheres in these visual representations. It should be noted that signal data can be readily computed at the centroid of each spherical surface panel as a function of time. This allows the representation of the complex vehicle signal characteristics on a simplified spherical surface, which can then be post-processed rather straightforwardly for far-field signal analysis. Clearly, through these types of graphical representations, one can achieve a very dynamic visualization of the change in acoustic pressure as a function of time on the surface of the sphere, namely, as the tips of the propeller blades make their closest passes to different segments of the sphere at various observer times.

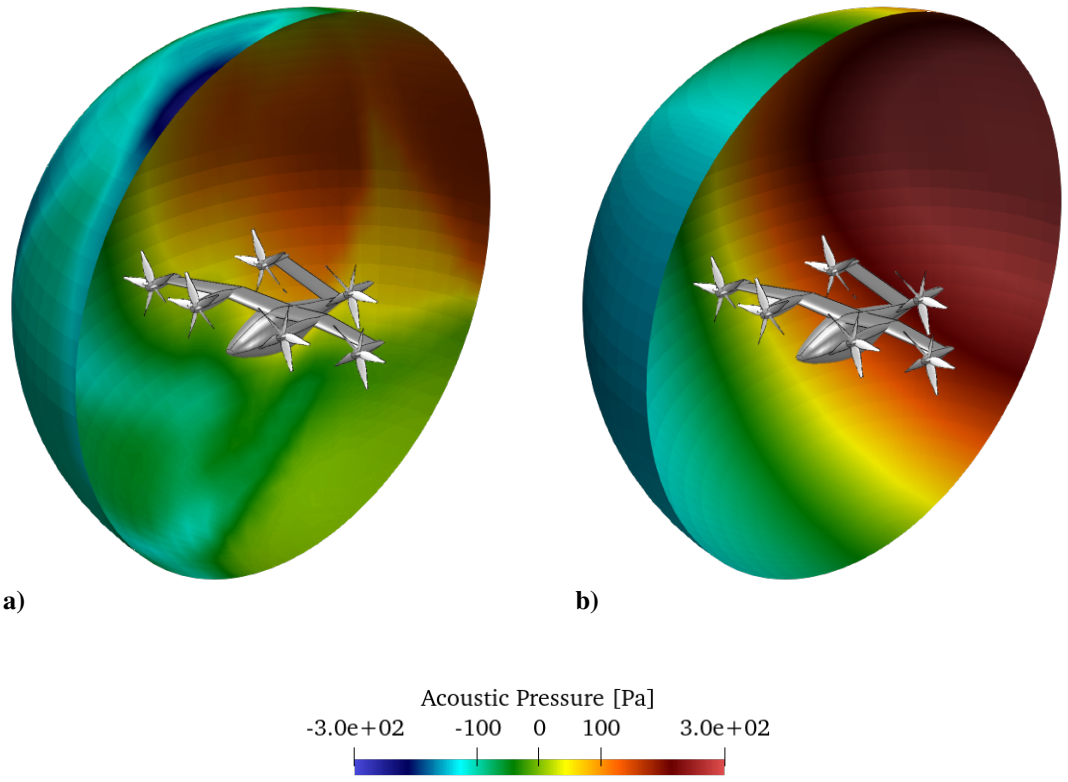

Fig. 13. Sample acoustic spheres around a Joby S4 UAM eVTOL vehicle with all six 5-bladed propellers operating synchronously in forward-flight mode. Acoustic pressure contours [Pa] are shown for the following time steps: a) $t = 0.04$ s and b) $t = 0.1$ s.

D. Case 3: DEP Vehicle with Multiple In-Phase Propellers

The last case study is performed on a pusher-propeller DEP UAM vehicle modeled using NASA OpenVSP around the Kittyhawk KH-H1 DEP vehicle depicted in Fig. 14. The purpose here is to demonstrate the differences in acoustic signatures from two highly dissimilar conceptual UAM/DEP designs relative to Cases 1 and 2. In a sense, demonstrating that FlightStream® can be effectively used to capture these vehicle-level differences may be viewed as a critical requirement for justifying its adoption in conceptual design.

The KH-H1 vehicle has eight pusher-type propellers in the forward-flight mode shown in Fig. 14. On the one hand, the two pairs of inboard wing propellers are operated at 1430 RPM with a tip Mach number of 0.2. On the other hand, the wingtip propellers are operated at a slightly higher angular speed of 1670 RPM with a tip Mach number of 0.25. As for the canard propellers, they are operated at the highest RPM of 1910, thus leading to a tip Mach number of 0.28. All propellers are allowed to operate synchronously. As a result, the entire vehicle is operated in forward-flight mode as further illustrated in Fig. 15. Therein, the interactions of the slipstream from the front canard propellers with the main wing and nacelles of the wing propellers are quite visible, along with the interference effects of the slipstream with the horizontal stabilizers.

As usual, 36 stationary microphones are placed in the form of a circular array at different range radii of 50 m, 100 m, and 150 m, respectively; these are positioned in a virtual plane that is dropped 4 m below the base of the vehicle fuselage and distributed equidistantly from the computed centroid of the vehicle. In this plane, the pressure signals are

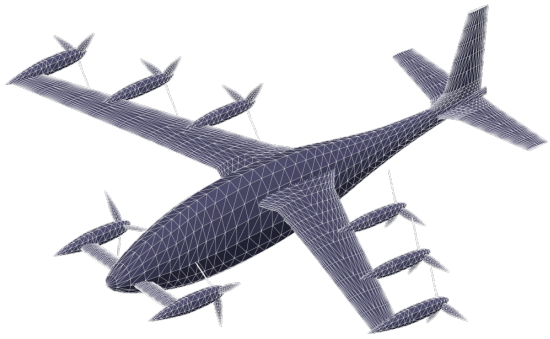

Fig. 14. Kittyhawk KH-H1 DEP vehicle with all eight propellers operating in forward-flight mode (Case 3).

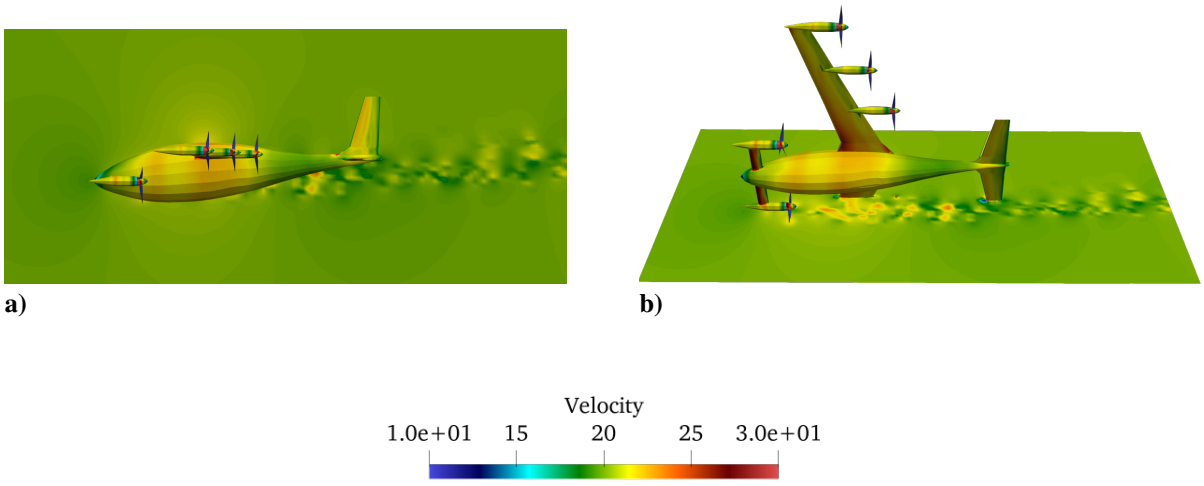

Fig. 15. FlightStream® simulations of a) side view and b) bottom view of the Kittyhawk KH-H1 DEP vehicle with all eight 3-bladed propellers operating synchronously in forward-flight mode (Case 3). The two pairs of inboard wing propellers operate at 1430 RPM with a tip $Ma = 0.2$. The wingtip propellers operate at 1670 RPM with $Ma = 0.25$. The canard propellers operate at 1910 RPM with $Ma = 0.28$. Everywhere, we set $\alpha = 5°$.

measured at discrete angular locations that vary from 0° to 360° in increments of 10°. These are computed and shown in Fig. 16 at 30° intervals.

As before, the flow moves horizontally in a direction from 180° → 0° into the propeller facing 180°. The variation in signal intensity and phase identification relative to Cases 1 and 2 is clear. Overall, signal characteristics that resemble those of Case 2 are realized. However, the presence of eight main propellers in operation compared to six, which actually rotate at three dissimilar blade revolution rates, can be seen to produce a highly jagged acoustic signal at the observer locations. This behavior may be inferred from the wide variety of tones detected. Moreover, the presence of distinct tonal spikes is no longer observed, and this may be attributed to the outcome of signal superposition being prescribed by the phase integrations of various contributing signals. At this juncture, should one be interested in identifying the dense harmonics comprising these signals, a frequency domain analysis will be required, as shown in Part 2 of this two-paper series.

For further illustration, acoustic volume sections of the Kittyhawk KH-H1 DEP vehicle with all eight 3-bladed propellers operating synchronously in forward-flight mode are provided in Fig. 17. Therein, the outer radius of the acoustic volume section is set at 15 m and the grid resolution is taken to be 40×40 in the radial and azimuthal directions, respectively. As before, using a blade pitch angle of $\alpha = 5°$ everywhere, the two pairs of inboard wing propellers are operated at 1430 RPM with a tip $Ma = 0.2$; the wingtip propellers are operated at 1670 RPM with $Ma = 0.25$; and the canard propellers are operated at 1910 RPM with $Ma = 0.28$. Figure 17 helps to visualize the acoustic field around the vehicle using the same orthogonal XYZ coordinate system convention; as before, the horizontal X and Y axes run parallel to the fuselage and wings, respectively, and Z represents the vertical direction. In the top view given by Fig. 17a, signal characteristics are captured in a plane situated at 5 m below the vehicle. In Fig. 17b, one may note a strong signal attenuation as we move to a plane situated 10 m below the vehicle. As usual, an acoustic noise bubble may be observed around the vehicle in the YZ plane, 3 m upstream of the vehicle's centroid (Fig. 17c). These visual aids are corroborated by the side view of the aircraft, which is taken at 8 m left of the aircraft, as shown in Fig. 17d.

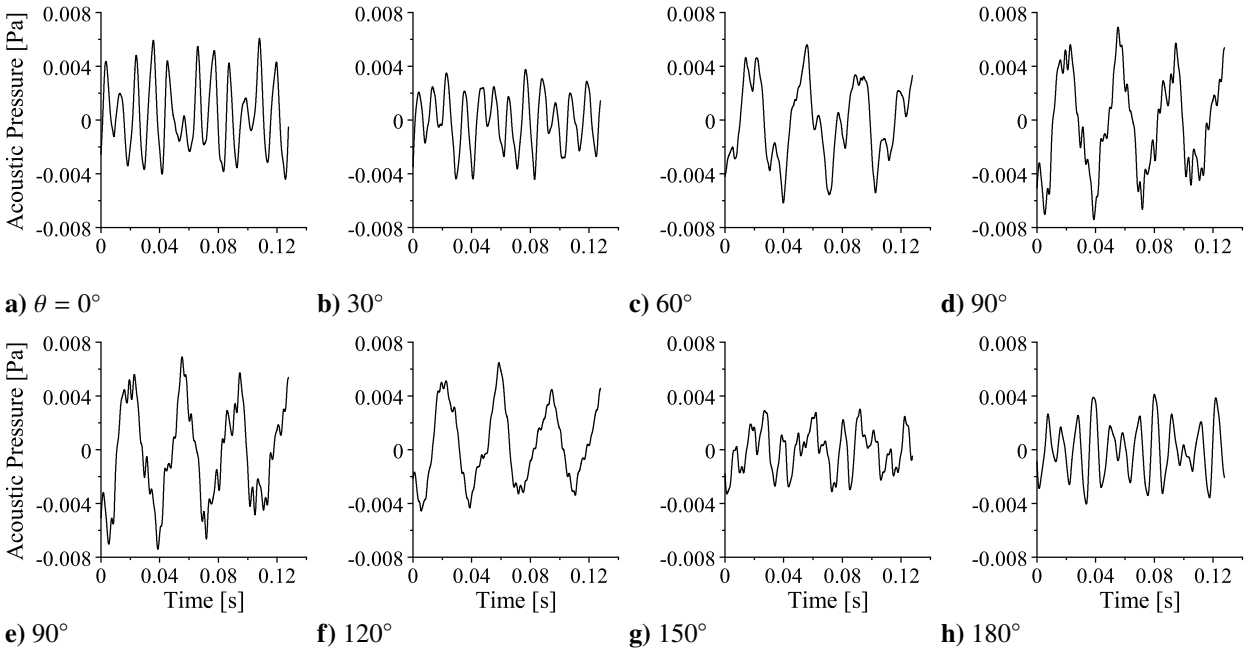

Fig. 16. Kittyhawk KH-H1 DEP vehicle with all eight propellers operating in forward-flight mode (Case 3). Acoustic pressure [Pa] signals provided at various distances from the vehicle's centroidal location are shown specifically at a) $\theta = 0°$, b) 30°, c) 60°, d) 90°, e) 90° (second row), f) 120°, g) 150°, and h) 180°.

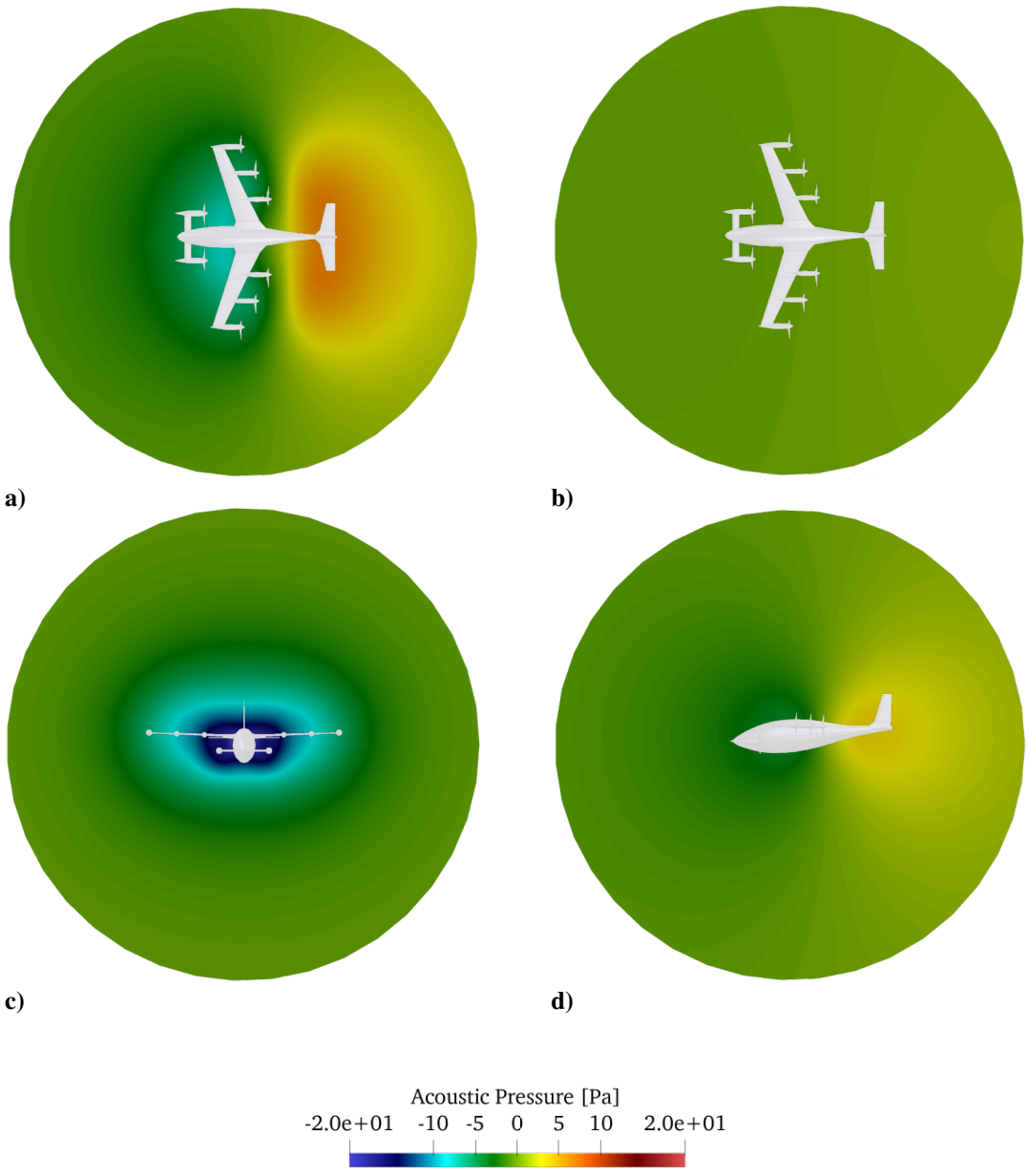

Fig. 17. Acoustic sections around a Kittyhawk KH-H1 DEP vehicle with all eight 3-bladed propellers operating synchronously in forward-flight mode using an outer radius of 15 m: a) Plane XY, 5 m below vehicle's centroid); b) Plane XY, 10 m below vehicle; c) Plane YZ, 3 m in front of the vehicle; and d) Plane XZ, 8 m left of vehicle.

IV. Conclusion

This study represents Part 1 of a two-paper series describing a NASA-funded activity in which the aeroacoustics Farassat Formulation 1A is successfully integrated into the commercial surface-vorticity solver, FlightStream®. The combination of a fast and user-friendly flow solver with an aeroacoustics toolbox has led to a capability in which UAM vehicles can be readily imported from a large variety of contemporary engineering tools. Given the high efficiency of the overarching framework, accurate solutions obtained in a matter of minutes are shown to include not only the flow characteristics, vorticity streaks, and loads all around the aircraft but also the acoustic signatures at essentially any observer point of interest. As part of this effort, extensive post processing tools have been systematically conceived and developed to aid the designer in meeting acoustic signature requirements. The underlying capability is further validated against several known UH-1H helicopter rotor experimental data obtained in both hover and forward-flight modes using both in-plane and out-of-plane detection planes. In all cases considered, the present simulation results are found to agree reasonably well with openly available experimental measurements. In this process, however, some known limitations of the F1A formulation are identified; these include its inability to resolve the high frequency broadband noise or capture the nonlinear quadrupole noise terms that become appreciable at high Mach numbers. Besides a preliminary study of NASA's RVLT Tiltwing UAM eVTOL vehicle with eight 5-bladed propellers, three specific UAM representative vehicles are selected to showcase the multi-rotor acoustic signal prediction capabilities. This is accomplished using extensive acoustic pressure characterization studies of the Joby S4 UAM eVTOL concept with either one or six synchronously operating 5-bladed propellers as well as the Kittyhawk KH-H1 DEP vehicle with eight 3-bladed propellers. Since this effort focuses on the strategic and programmatic implementation of the F1A formulation, the frequency domain decomposition, post processing, and evaluation of several certification-driven acoustic metrics of interest to the FAA and ICAO are pursued separately in a companion article.

Acknowledgments

The authors wish to acknowledge the cooperation and support of the NASA researchers and the NASA SBIR Office for this effort. The primary work for this paper was performed within the context of the NASA STTR 80NSSC20C0586 Phase I contract activity.

References

[1] Whittle, R., "Air Mobility Bonanza Beckons Electric VTOL Developers," *Vertiflite*, Vol. 2, March-April 2017, pp. 14–21.

[2] Swartz, K., "Charging Forward New eVTOL Concepts Advance," *Vertiflite*, Vol. 4, July-August 2017, pp. 24–29.

[3] "NASA Aeronautics Strategic Plan, 2017 Update," Technical Report NASA Report No. NP-2017-01-2352-HQ, National Aeronautics and Space Administration, NASA Headquarters, Washington, DC, 2017.

[4] Jia, Z. and Lee, S., "Acoustic Analysis of a Quadrotor eVTOL Design Via High-fidelity Simulations," *2019 AIAA/CEAS Aeroacoustics Conference*, AIAA Paper 2019-2631, May 2019. doi:10.2514/6.2019-2631.

[5] Lee, H. and Lee, D.-J., "Rotor Interactional Effects on Aerodynamic and Noise Characteristics of a Small Multirotor Unmanned Aerial Vehicle," *Physics of Fluids*, Vol. 32, No. 4, April 2020, pp. 047107. doi:10.1063/5.0003992.

[6] Gwak, D. Y., Han, D., and Lee, S., "Sound Quality Factors Influencing Annoyance from Hovering UAV," *Journal of Sound and Vibration*, Vol. 489, December 2020, pp. 115651. doi:10.1016/j.jsv.2020.115651.

[7] Smith, D. A., Filippone, A., and Bojdo, N., "Noise Reduction of a Counter Rotating Open Rotor through a Locked Blade Row," *Aerospace Science and Technology*, Vol. 98, March 2020, pp. 105637. doi:10.1016/j.ast.2019.105637.

[8] Krishnamurthy, S., Rizzi, S. A., Cheng, R., Boyd, D. D., and Christian, A. W., "Prediction-based Auralization of a Multirotor Urban Air Mobility Vehicle," *2021 AIAA SciTech Forum*, AIAA Paper 2021-0587, January 2021. doi:10.2514/6.2021-0587.

[9] Jeong, J., Ko, J., Cho, H., and Lee, S., "Random Process-based Stochastic Analysis of Multirotor Hovering Noise Under Rotational Speed Fluctuations," *Physics of Fluids*, Vol. 33, No. 12, December 2021, pp. 127107. doi:10.1063/5.0071850.

[10] Dbouk, T. and Drikakis, D., "Quadcopter Drones Swarm Aeroacoustics," *Physics of Fluids*, Vol. 33, No. 5, May 2021, pp. 057112. doi:10.1063/5.0052505.

[11] Ko, J., Jeong, J., Cho, H., and Lee, S., "Real-Time Prediction Framework for Frequency-Modulated Multirotor Noise," *Physics of Fluids*, Vol. 34, No. 2, February 2022, pp. 027103. doi:10.1063/5.0081103.

[12] Wang, X., Wang, Y., Wang, P., Yang, S., Niu, W., and Yang, Y., "Design, Analysis, and Testing of Petrel Acoustic Autonomous Underwater Vehicle for Marine Monitoring," *Physics of Fluids*, Vol. 34, No. 3, March 2022, pp. 037115. doi:10.1063/5.0083951.

[13] Li, S. and Lee, S., "Prediction of Urban Air Mobility Multirotor VTOL Broadband Noise Using UCD-QuietFly," *Journal of the American Helicopter Society*, Vol. 66, No. 3, July 2021, pp. 1–13. doi:10.4050/jahs.66.032004.

[14] Ahuja, V., Burkhalter, J., and Hartfield, R. J., "Robust Prediction of High Lift Using Surface Vorticity – Phase II Final Report," Technical Report NASA SBIR Report No. NNX17CL12C, Research in Flight Company, LLC, Opelika, AL, 2017.

[15] Lowson, M. V., "The Sound Field for Singularities in Motion," *Proceedings of the Royal Society of London. Series A. Mathematical and Physical Sciences*, Vol. 286, No. 1407, 1965, pp. 559–572. doi:10.1098/rspa.1965.0164.

[16] Brentner, K. S. and Farassat, F., "Helicopter Noise Prediction: The Current Status and Future Direction," *Journal of Sound and Vibration*, Vol. 170, No. 1, February 1994, pp. 79–96. doi:10.1006/jsvi.1994.1047.

[17] Brentner, K. S. and Farassat, F., "Modeling Aerodynamically Generated Sound of Helicopter Rotors," *Progress in Aerospace Sciences*, Vol. 39, No. 2-3, 2003, pp. 83–120. doi:10.1016/S0376-0421(02)00068-4.

[18] Ahuja, V. and Hartfield, R. J., "Aerodynamic Loads over Arbitrary Bodies by Method of Integrated Circulation," *Journal of Aircraft*, Vol. 53, No. 6, November 2016, pp. 1719–1730. doi:10.2514/1.c033619.

[19] DiMaggio, G. A., Hartfield, R. J., Majdalani, J., and Ahuja, V., "Solid Rocket Motor Internal Ballistics Using an Enhanced Surface-Vorticity Panel Technique," *Physics of Fluids*, Vol. 33, No. 10, October 2021, pp. 103613–16. doi:10.1063/5.0069075.

[20] Ffowcs Williams, J. E. and Hawkings, D., "Sound Generation by Turbulence and Surfaces in Arbitrary Motion," *Philosophical Transactions of the Royal Society of London. Series A, Mathematical and Physical Sciences*, Vol. 264, No. 1151, 1969, pp. 321–342. doi:10.1098/rsta.1969.0031.

[21] Farassat, F., "Derivation of Formulations 1 and 1A of Farassat," Technical Report NASA Technical Memorandum No. TM-2007-214853, National Aeronautics and Space Administration, NASA Langley Research Center, Hampton, VA, 2007.

[22] Maskew, B., "A Quadrilateral Vortex Method Applied to Configurations with High Circulation," Technical Report NASA Scientific Paper No. SP-406, N76-28173, NASA Workshop on Vortex-Lattice Utilization, NASA Langley Research Center, Hampton, VA, May 1976.

[23] Dvorak, F. A., Woodward, F. A., and Maskew, B., "A Three-Dimensional Viscous/Potential Flow Interaction Analysis Method for Multi-Element Wings," Technical Report NASA Contractor Report No. CR-152012, N77-27076, National Aeronautics and Space Administration, NASA Headquarters, Washington, DC, August 1977.

[24] Maskew, B., "Program VSAERO Theory Document," Technical Report NASA Contractor Report No. CR-4023, N77-27076, National Aeronautics and Space Administration, NASA Headquarters, Washington, DC, September 1987.

[25] Katz, J. and Plotkin, A., *Low Speed Aerodynamics*, Cambridge University Press, New York, NY, 2nd ed., 2001.

[26] Wu, J.-Z., Ma, H.-Y., and Zhou, M.-D., *Vorticity and Vortex Dynamics*, Springer, Berlin, May 2006.

[27] Ahuja, V., Burkhalter, J., and Hartfield, R. J., "Early-Design Aeroacoustics Prediction for Distributed Electric Propulsion Vehicles Using FlightStream® – Phase I Final Report," Technical Report NASA STTR Report No. 80NSSC20C0586, Research in Flight Company, LLC, Auburn, AL, 2020.

[28] Faure, T. M. and Leogrande, C., "High Angle-of-attack Aerodynamics of a Straight Wing with Finite Span Using a Discrete Vortex Method," *Physics of Fluids*, Vol. 32, No. 10, October 2020, pp. 104109. doi:10.1063/5.0025327.

[29] Faure, T. M., Roncin, K., Viaud, B., Simonet, T., and Daridon, L., "Flapping Wing Propulsion: Comparison Between Discrete Vortex Method and Other Models," *Physics of Fluids*, Vol. 34, No. 3, March 2022, pp. 034108. doi:10.1063/5.0083158.

[30] Fenyvesi, B., Kriegseis, J., and Horváth, C., "An Automated Method for the Identification of Interaction Tone Noise Sources on the Beamforming Maps of Counter-rotating Rotors," *Physics of Fluids*, Vol. 34, No. 4, April 2022, pp. 047105. doi:10.1063/5.0083634.

[31] Olson, E. D. and Albertson, C. W., "Aircraft High-Lift Aerodynamic Analysis Using a Surface-Vorticity Solver," *54th AIAA Aerospace Sciences Meeting*, AIAA Paper No. 2016-0779, San Diego, California, January 2016. doi:10.2514/6.2016-0779.

[32] Sandoz, B., Ahuja, V., and Hartfield, R. J., "Longitudinal Aerodynamic Characteristics of a V/STOL Tilt-wing Four-Propeller Transport Model Using a Surface Vorticity Flow Solver," *2018 AIAA Aerospace Sciences Meeting*, AIAA Paper No. 2018-2070, Kissimmee, Florida, January 2018. doi:10.2514/6.2018-2070.

[33] Cheng, H., Greengard, L., and Rokhlin, V., "A Fast Adaptive Multipole Algorithm in Three Dimensions," *Journal of Computational Physics*, Vol. 155, No. 2, November 1999, pp. 468–498. doi:10.1006/jcph.1999.6355.

[34] Thwaites, B., "Approximate Calculation of the Laminar Boundary Layer," *Aeronautical Quarterly*, Vol. 1, No. 3, November 1949, pp. 245–280. doi:10.1017/s0001925900000184.

[35] White, F. M. and Majdalani, J., *Viscous Fluid Flow*, McGraw-Hill, New York, NY, 4th ed., 2021.

[36] Standen, N. M., *Calculation of Integral Parameters of a Compressible Turbulent Boundary Layer Using a Concept of Mass Entrainment*, Master's thesis, Department of Mechanical Engineering, McGill University, Montreal, Canada, August 1964.

[37] Metzger, F. B., "A Review of Propeller Noise Prediction Methodology: 1919-1994," Technical Report NASA Contractor Report No. CR-198156, National Aeronautics and Space Administration, NASA Langley Research Center, Hampton, VA, June 1995.

[38] Shirey, J., Brentner, K., and Chen, H.-n., "A Validation Study of the PSU-WOPWOP Rotor Noise Prediction Code," *45th AIAA Aerospace Sciences Meeting and Exhibit*, AIAA Paper No. 2007-1240, Reno, Nevada, January 2007. doi:10.2514/6.2007-1240.

[39] Conner, D. A. and Hoad, D. R., "Reduction of High-Speed Impulsive Noise by Blade Planform Modification of a Model Helicopter Rotor," Technical Report NASA Technical Memorandum No. TM-84553, National Aeronautics and Space Administration, NASA Langley Research Center, Hampton, VA, 1982.

[40] Dunn, M. H. and Tarkenton, G. M., "Computational Methods in the Prediction of Advanced Subsonic and Supersonic Propeller Induced Noise: ASSPIN Users' Manual," Technical Report NASA Contractor Report No. CR-4434, National Aeronautics and Space Administration, NASA Langley Research Center, Hampton, VA, 1992.

[41] Lopes, L. and Burley, C., "Design of the Next Generation Aircraft Noise Prediction Program: ANOPP2," *17th AIAA/CEAS Aeroacoustics Conference (32nd AIAA Aeroacoustics Conference)*, AIAA Paper No. 2011-2854, Portland, Oregon, June 2011. doi:10.2514/6.2011-2854.

[42] Opoku, D. G., Triantos, D. G., Nitzsche, F., and Voutsinas, S. G., "Rotorcraft Aerodynamic and Aeroacoustic Modelling Using Vortex Particle Methods," *2002 International Congress of Aeronautical Sciences Conference*, 2002, pp. 8–13.